< Electronic Supporting Information>

Accurate Binding of Porous Aluminum Molecular Ring Catalyst with the Substrate

Dan Luo[+], Han Xiao[+], Min-Yi Zhang, Shang-Da Li, Liang He, Hong Lv, Chun-Sen Li, Qi-Pu Lin, Wei-Hui Fang* and Jian Zhang

[*] Dan Luo[+], Han Xiao[+], Min-Yi Zhang, Shang-Da Li, Liang He, Hong Lv, Chun-Sen Li, Qi-Pu Lin, Wei-Hui Fang* and Jian Zhang
State Key Laboratory of Structural Chemistry
Fujian Institute of Research on the Structure of Matter,
Chinese Academy of Sciences, Fuzhou, Fujian 350002, P. R. China.
E-mail: fwh@fjirsm.ac.cn
Han Xiao[+]
University of Chinese Academy of Sciences, Beijing 100049, China
Chun-Sen Li
Fujian Provincial Key Laboratory of Theoretical and Computational Chemistry, Xiamen, Fujian 361005, China
[+] these authors contributed equally to this work.

Content

1.Experimental

Materials and Methods.

All the reagents and solvents were purchased commercially and were used without further purification. 3-aminoisonicotinic acid (NH_2-HIN) (≥97%) was acquired from Adamas-beat. Aluminum isopropoxide (≥98%) is bought from Aladdin Chemical Reagent Shanghai. N, N-dimethylformamide (DMF, ≥99.5%), n-BuOH (≥99.5%), and toluene (≥99.5%) were acquired from Sinopharm Chemical Reagent Beijing.

Synthesis of the AlOCs.

Pale yellow cubic crystals of compound $[Al_8(OH)_4(OBu^n)_8(NH_2\text{-}IN)_{12}]$ (**AlOC-58NC**) were synthesized via a solvothermal reaction of aluminum isopropoxide (204 mg, 1 mmol), 3-aminoisonicotinic acid (210 mg, 1.52 mmol) in a mixed solvent containing n-butanol (2.5 mL) and DMF (2.5 mL) at 100 °C for 4 days. Light yellow strip-like crystals of compound $[Al_8(OH)_8(NH_2\text{-}IN)_{16}]$ (**AlOC-59NT**) were obtained by removing alcohol from the reaction system and replacing it with toluene with the help of an auxiliary solvent (methylamine ethanol solution, 40%).

X-ray Crystallography.

Single crystal X-ray diffraction data of AlOCs and aromatic aldehydes-loaded **AlOC-59NT** were collected on Hybrid Pixel Array detector equipped with Ga-Kα radiation (λ=1.3405 Å) at about 100K. The structures were solved with the dual-direct methods using ShelxT and refined with the full-matrix least-squares technique based on F^2 using the SHELXL.[1] Non-hydrogen atoms were refined anisotropically. Hydrogen atoms were added theoretically, riding on the concerned atoms and refined with fixed thermal factors. All absorption corrections were performed using the multi-scan program. And n-butyl alcohol molecules are severely disordered and the related hydrogen atoms were not included in **AlOC-58NC**. The oxygen atoms of aromatic aldehydes are disordered in aromatic aldehydes-loaded **AlOC-59NT**. The obtained crystallographic data are summarized in Tables S7-S8.

Thermogravimetric Analysis (TGA).

TGA was performed on a Mettler Toledo TGA/SDTA 851^e analyzer in N_2 with a heating rate of 10 °C min^{-1} from 20 to 800 °C.

Fourier Transform Infrared (FT-IR) Spectroscopy.

IR spectra (KBr pellets) were recorded on an ABB Bomem MB102 spectrometer over a range 400-4000 cm^{-1}.

UV-vis spectroscopy.

The UV-vis diffuse reflection data were recorded at room temperature using a powder sample with $BaSO_4$ as a standard (100 % reflectance) on a Perkin Elmer Lamda-950 UV spectrophotometer and scanned at 200-800 nm.

Element Analysis.

The energy dispersive spectroscopy (EDS) analyses were performed on a JEOL JSM6700F field-emission scanning electron microscope equipped with an Oxford INCA system. Elemental analysis (C, N, H) was carried out on a Vario Micro E III analyzer.

Nuclear magnetic spectrum.

^{1}H NMR spectra were recorded on a Bruker AVANCE III spectrometer (400 MHz) or a JEOL ECZ600S spectrometer (600 MHz).

Powder X-ray diffraction (PXRD) and temperature-dependent PXRD.

Single crystal samples of compounds **AIOC-58NC** and **AIOC-59NT** were grinded in a mortar and sieved with a 200 molybdenum sieve and then used for testing. PXRD data were collected on a Rigaku SmartLab X-ray thin-film diffractometer with Cu Kα radiation (λ = 1.54 Å). Molecular modeling was carried out using Reflex Plus, a module implemented in Materials Studio (version 4.4) by Accelrys Inc. The initial structures were constructed piecewise starting with a cubic cell with space group *I*432 for **AIOC-58NC** and a tetragonal cell with space group *I*422 for **AIOC-59NT**. For **AIOC-58NC**, the Tomandl Pseudo-Voigt function was used for whole profile fitting and Berrar-Baldinozzi function was used for asymmetry correction during the refinement processes. For **AIOC-59NT**, the Gaussian function was used for whole profile fitting and Berrar-Baldinozzi function was used for asymmetry correction during the refinement processes. The PXRD patterns of **AIOC-59NT** were verified by the Rietveld and Pawley refinement methods, respectively. Temperatures-dependent PXRD data were collected on a Rigaku Ultima-IV diffractometer using Cu-Kα radiation (λ = 1.54056 Å) under 25 °C to 250 °C.

General procedure and catalytic recycling of AIOCs-catalyzed cyanosilylation.

The mixture of aldehyde, trimethylsilyl cyanide (TMSCN) and CH_2Cl_2 was added to the schlenk tube (0.5mmol aldehyde, 1mmol of TMSCN and 5mL CH_2Cl_2), where the activated AIOCs had been introduced in advance. The mixture was stirred (260 rpm) at room temperature for 2 h, under N_2 atmosphere. For comparison, all tested substrates were tested under the same standard conditions. Yields were determined by ^{1}H-NMR analysis using CH_2Br_2 as an internal standard. After the reaction, AIOCs were separated from the reaction mixture by suction filtration. The filtrate containing the reaction product was removed and the AIOCs were washed by repeated additions of ethyl acetate (3×1mL) and then centrifuged. After the purification operation, the AIOCs were dried and used in the next reaction.

Computational details

Molecular dynamics simulation with GFN-Force-Field,[2] and geometry optimization at GFN0-xTB[3] level are performed using the xTB package.[4] Four- and six-monomers clusters (Fig. S45) are abstracted from the nanotube **AIOC-59NT** and nanocage **AIOC-58NC** crystal structures, respectively, for modeling to determine adsorption sites and calculate adsorption energies. In order to conserve the crystal structures during geometry optimization, N, O, Al in **AIOC-58NC** and N, Al in **AIOC-59NT** are constrained by a force constant of 25.0 Hartree/Bohr^2. Adsorption energy E_{ads} are performed using eq. 1, where C and S denote cluster and substrate respectively, and the energy is derived from a single point calculation at GFN2-xTB[5] level. To determine the Lewis acid/base character of **AIOC-58NC** and **AIOC-59NT**, monomers are isolated from the

crystal structure and geometric optimization at GFN2-xTB level is performed. Then, single-point calculations at TPSSh[6] /def2-SVP[7] level for individual molecules in **AlOC-58NC** and **AlOC-59NT** are performed using ORCA package.[8] Multiwfn[9] is used to analyze the wave function produced by single point energy calculations, and investigate weak interaction by the interaction region indicator (IRI)[10] method.

$$E_{ads} = E_{C+S} - E_C - E_S$$

2.Synthesis

Synthesis of AlOC-58NC

A mixture of aluminum isopropoxide (204 mg, 1 mmol), 3-aminoisonicotinic acid (210 mg, 1.52 mmol); n-butanol (2.5 mL) and DMF (2.5 mL) was sealed in a 20 mL vial and transferred to a preheated oven at 100 °C for 4 days. When cooled to room temperature, pale yellow cubic crystals were obtained. The crystals are rinsed with DMF and preserved under a sealed and dry environment. (yield: 75% based on $Al(O^iPr)_3$). FT-IR (KBr, cm^{-1}): 3456(s), 3345(s), 3212(m), 2953(m), 2865(m), 1665(s), 1606(s), 1575(s), 1533(s), 1461(s), 1401s). Elemental analysis calcd. (%) for $Al_8C_{104}N_{24}O_{38}H_{140}$ (MW 2550.21): C 48.98, N 13.25, H 5.53; found C 48.96, N 12.62, H 5.46.

Synthesis of AlOC-59NT

A mixture of aluminum isopropoxide (204 mg, 1 mmol), 3-aminoisonicotinic acid (210 mg, 1.52 mmol); methylamine ethanol solution (40 %, 120 μL), toluene (3 mL) and DMF (3 mL) was sealed in a 20 mL vial and transferred to a preheated oven at 100 °C for 5 days. When cooled to room temperature, pale yellow strip crystals were obtained. (yield: 70 % based on $Al(O^iPr)_3$). The crystals are rinsed with DMF and preserved under a sealed and dry environment. FT-IR (KBr, cm^{-1}): 3754(w), 3442(w), 3323(w), 3184(w), 3110(w), 2945(w), 1654(m), 1615(m), 1578(s), 1527(m), 1456(s), 1402(s), 1234.52(s). Elemental analysis calcd. (%) for $Al_8C_{96}N_{32}O_{40}H_{88}$ (MW 2545.76): C 45.29, N 17.61, H 3.48; found C 44.35, N 15.12, H 4.60.

3.The structure information for AlOCs

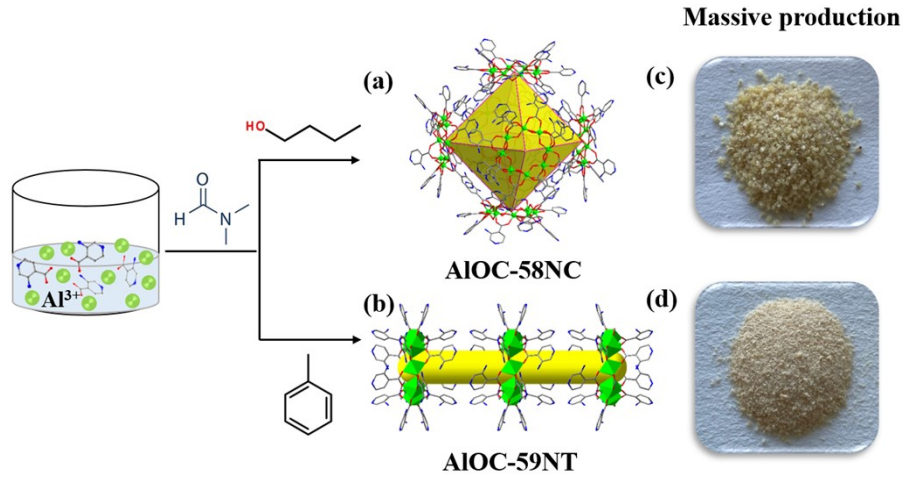

Figure S1. Synthetic regulation. (a) Preparation of nanocage structure **AlOC-58NC** from coordination alcohol. (b) Preparation of nanotubes **AlOC-59NT** from uncoordinated toluene. The massive production of (c) **AlOC-58NC** and (d) **AlOC-59NT.** Color code: Al, green; C, black; O, red; N, blue.

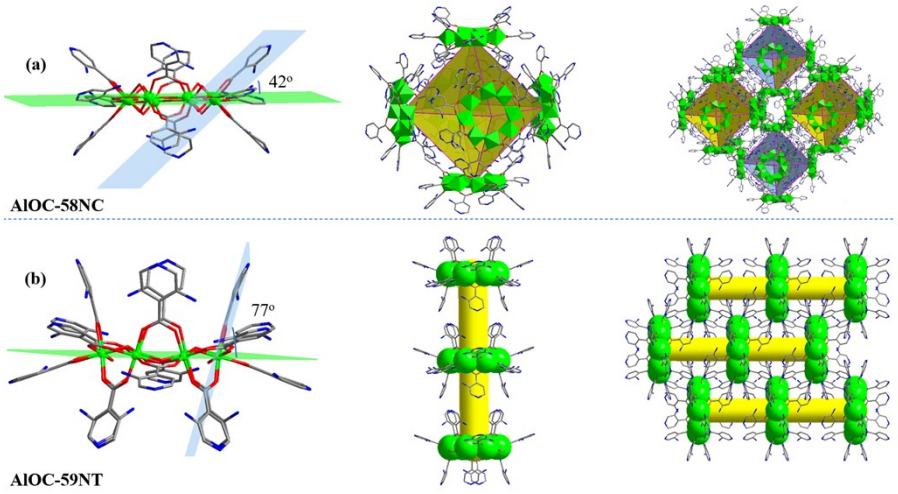

Figure S2. (a) Molecular ring, nanocage and packing view of **AlOC-58NC**. (b) Molecular ring, nanotube and packing view of **AlOC-59NT**.

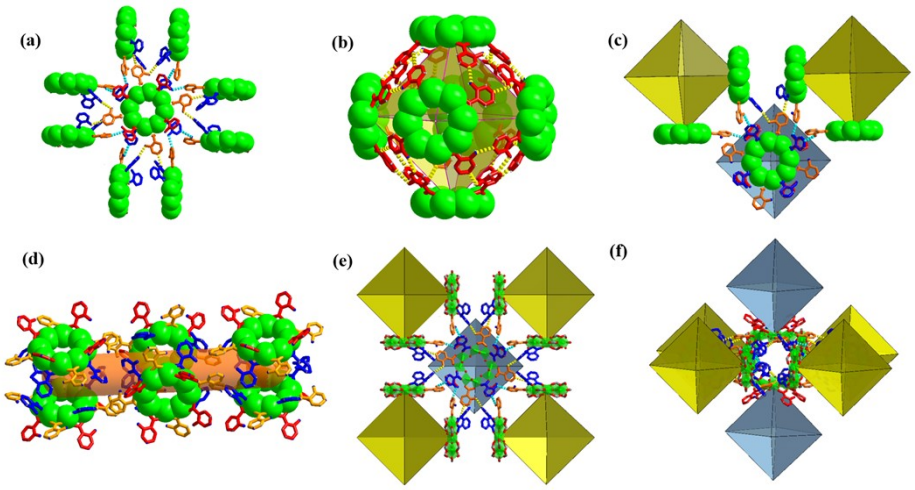

Figure S3. The role of α, β and γ in the nanocages of **AlOC-58NC**. (a) The interaction force between α, β and γ on the nanocage and the adjacent nanocage. (b) The nanocage formed between α position ligands through N-H···N hydrogen bond. (c) Hydrogen bond interactions between β, γ and adjacent nanocages. (d) The micropores formed between γ position ligands through N-H···N hydrogen bond. (e) The interaction forces between β, γ and adjacent nanocages. (f) Spatially staggered stacking diagram between nanocages (yellow and blue represent nanocages located in the equator and axial planes, respectively). Some carbon and hydrogen atoms have been omitted for clarity. Color code: Al, green; C, black; O, red; N, blue.

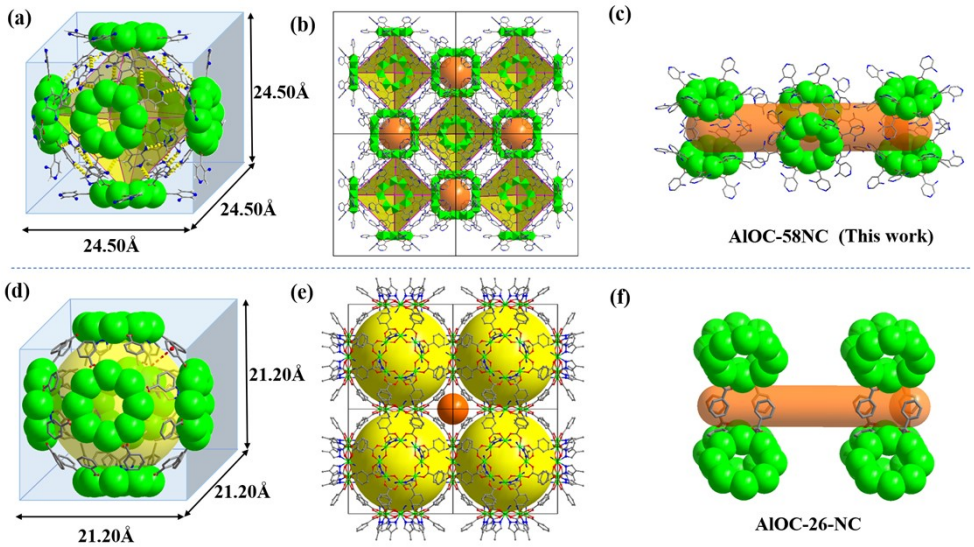

Figure S4. The comparison between nanocages of **AlOC-58NC** and **AlOC-26-NC**. (a) Octahedral cage structure of compound **AlOC-58NC** linked by N-H···N hydrogen bonds (3.00 Å). (b) Stacked diagram of nanocages, cages are arranged in -ABAB- alternation. (c) Micropores are composed of four staggered molecular rings (size: 6.65 Å). (d) Cubic cage structure of compound **AlOC-26-NC** linked by π···π (4.05 Å). (e) Stacked diagram of nanocages, cages arranged in –AAA- alternation. (f) Micropores are composed of aromatic ligands on molecular rings (size: 7.80 Å). Color code: Al, green; C, black; O, red; N, blue.

The comparison between nanocages of AlOC-58NC and AlOC-26-NC[11]

The supramolecular nanocages structure of **AlOC-58NC** is similar to previously reported **AlOC-26-NC**, but differs in the following three points. First is the ring type, **AlOC-58NC** belongs to type II while **AlOC-26-NC** belongs to type III. Secondly, the way of assembly between the rings is different. In **AlOC-58NC**, six eight-membered rings are connected by N-H···N hydrogen bonding interactions (3.00 Å) to form nanocage, while those in **AlOC-26-NC** are considerably weak π···π interactions (4.01 Å) and C-H···C hydrogen bonding interactions (4.00 Å). Finally, their supramolecular packing is also unlike. Compared with the reported -AA- stacking, compound **AlOC-58NC** adopts -ABAB- alternation. Therefore, the distance between adjacent cages (36.69 Å vs 21.20 Å) and the shape of the microporous formed are also disparate. In addition, the size of the micropores in **AlOC-58NC** is slightly smaller (6.65 Å vs 7.80 Å) and is composed of four staggered Al_8 rings compared to the aromatic ligands on the ring.

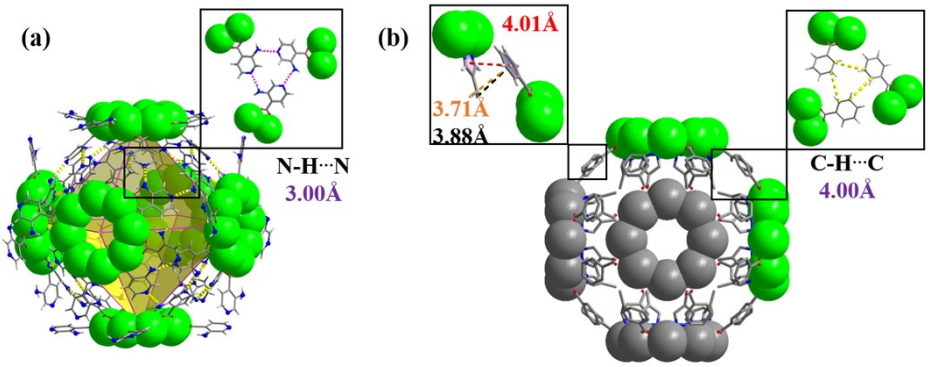

Figure S5. The comparison of interactions between molecular rings in **AlOC-58** and **AlOC-26-NC**: (a) The N-H···N hydrogen bond interactions in **AlOC-58NC;** (b) The C-H···π and π···π interactions in **AlOC-26-NC**.

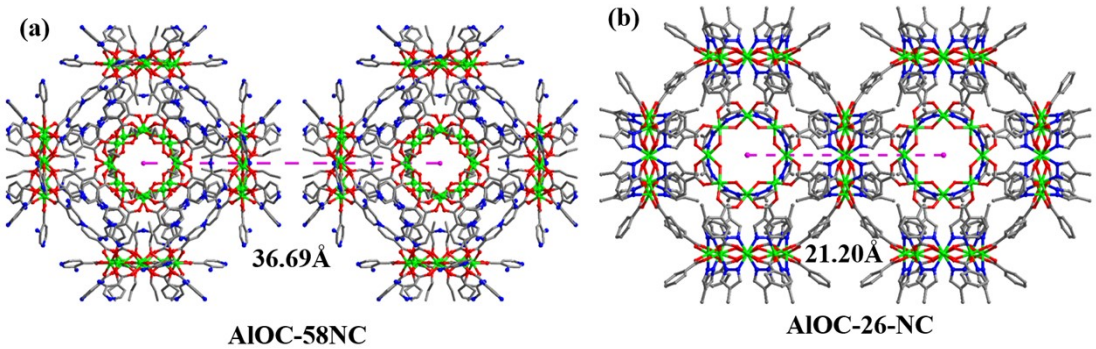

Figure S6. The comparison of the cage-to-cage distance between **AlOC-58NC** and **AlOC-26-NC**.

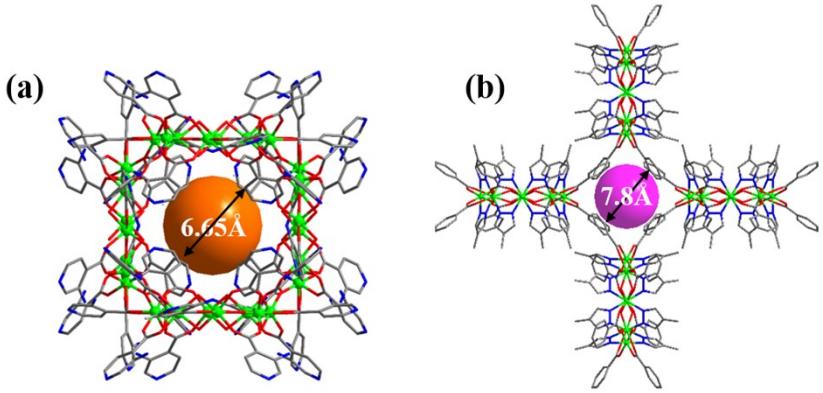

Figure S7. The comparison of micropore aperture composition between **AlOC-58NC** and **AlOC-26-NC.**

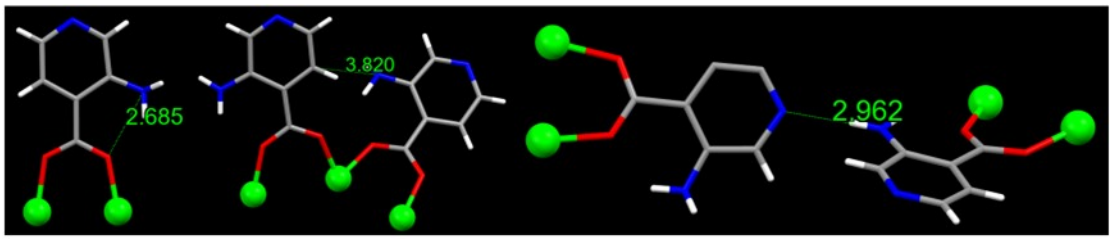

Figure S8. The hydrogen bond interactions in **AlOC-58NC**. Color code: Al, green; O, red; C, gray; N, blue.

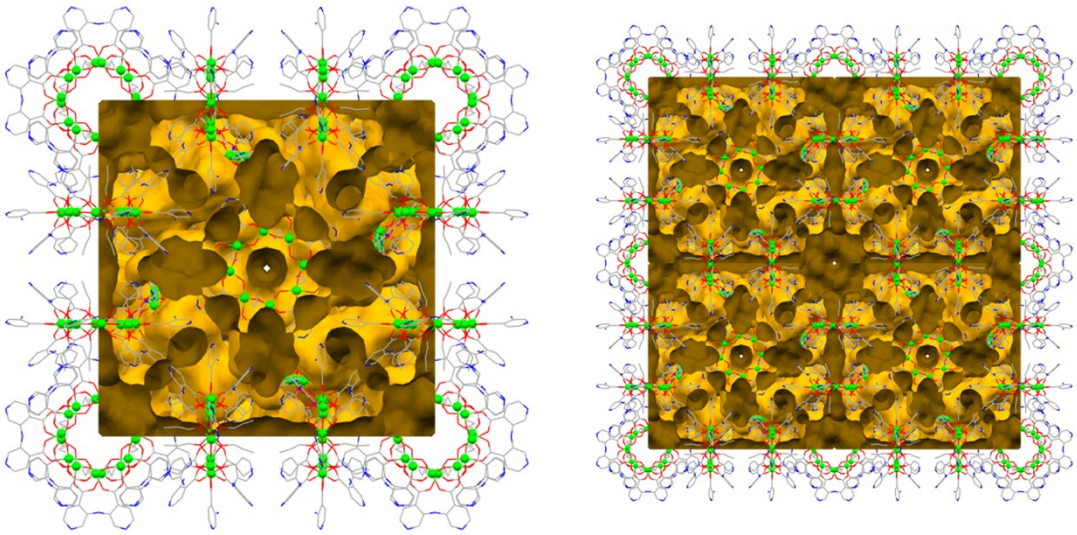

Figure S9. Perspective view of the void spaces in **AlOC-58NC** with unit cell (left) and 2×2×2 stacking (right).

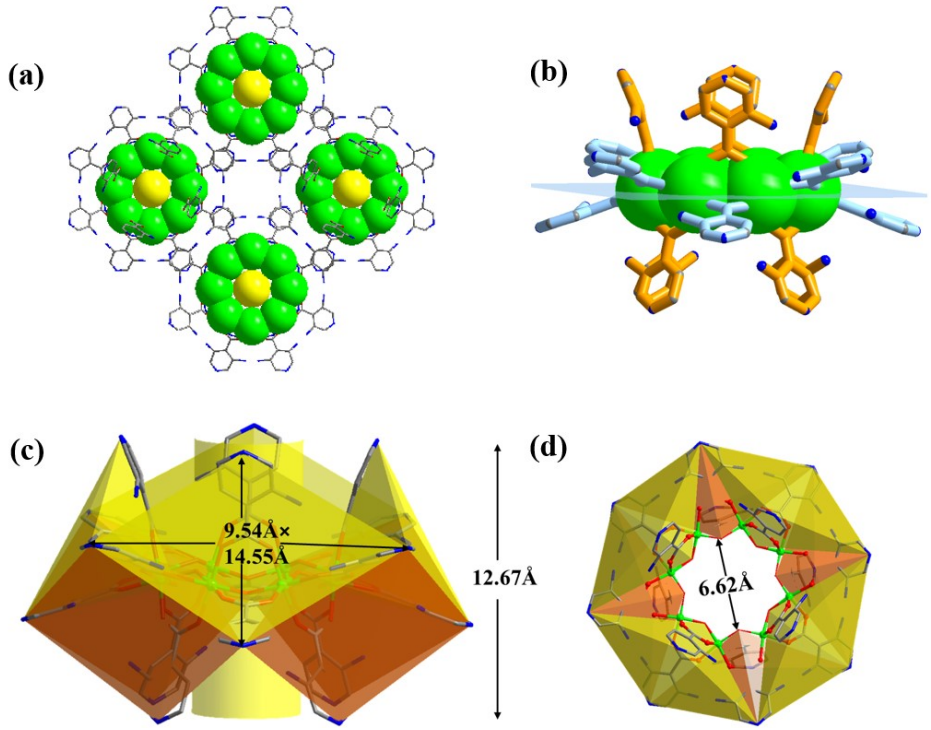

Figure S10. (a) Stacking diagram of a nanotube array; (b) The side view of the ring structure. (c) The dimensions of the half-open cavity; (d) The dimension of the hollow tubular cavity in **AlOC-59NT**.

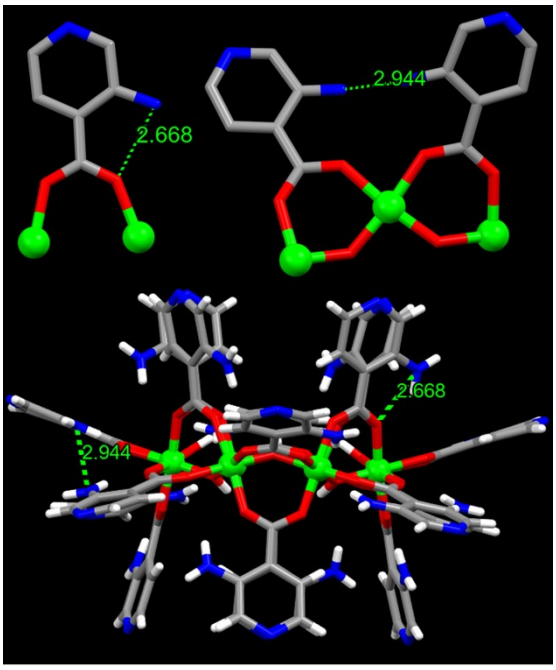

Figure S11. The hydrogen bond interactions in **AlOC-59NT**. Color code: Al, green; O, red; C, gray; N, blue.

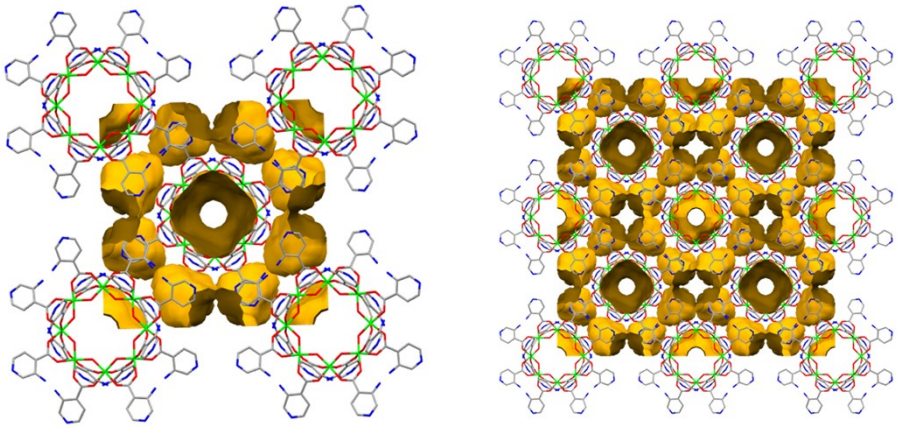

Figure S12. Perspective view of the void spaces in **AlOC-59NT** with unit cell (left) and 2×2×2 stacking (right).

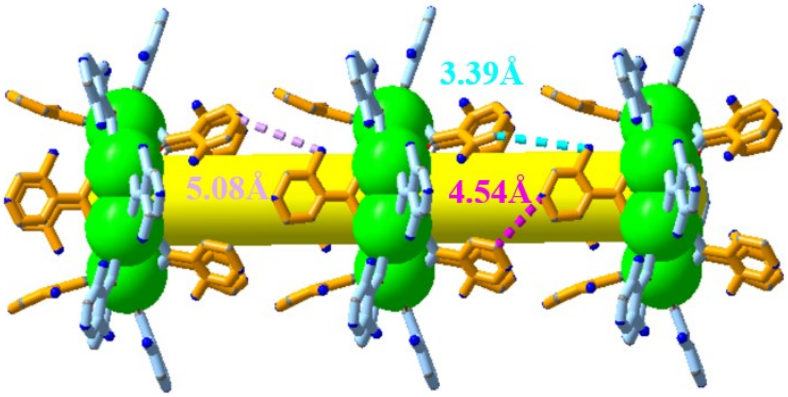

Figure S13. The interaction force between aromatic ligands on the same nanotubes in **AlOC-59NT**.

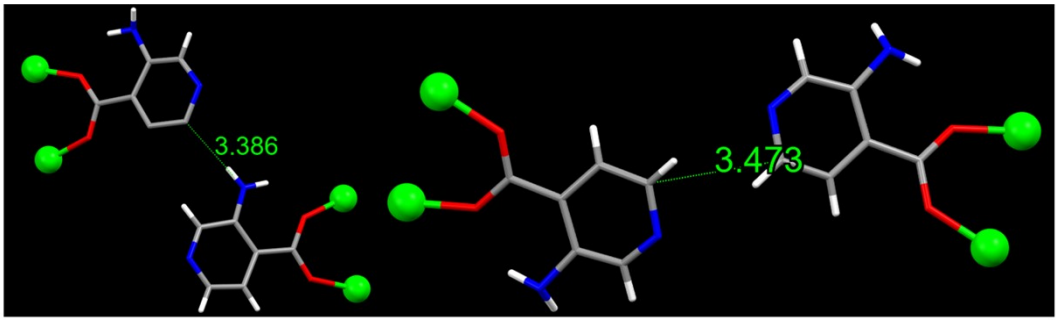

Figure S14. The interaction force between adjacent molecular rings on the same nanotube in **AlOC-59NT**. Color code: Al, green; O, red; C, gray; N, blue.

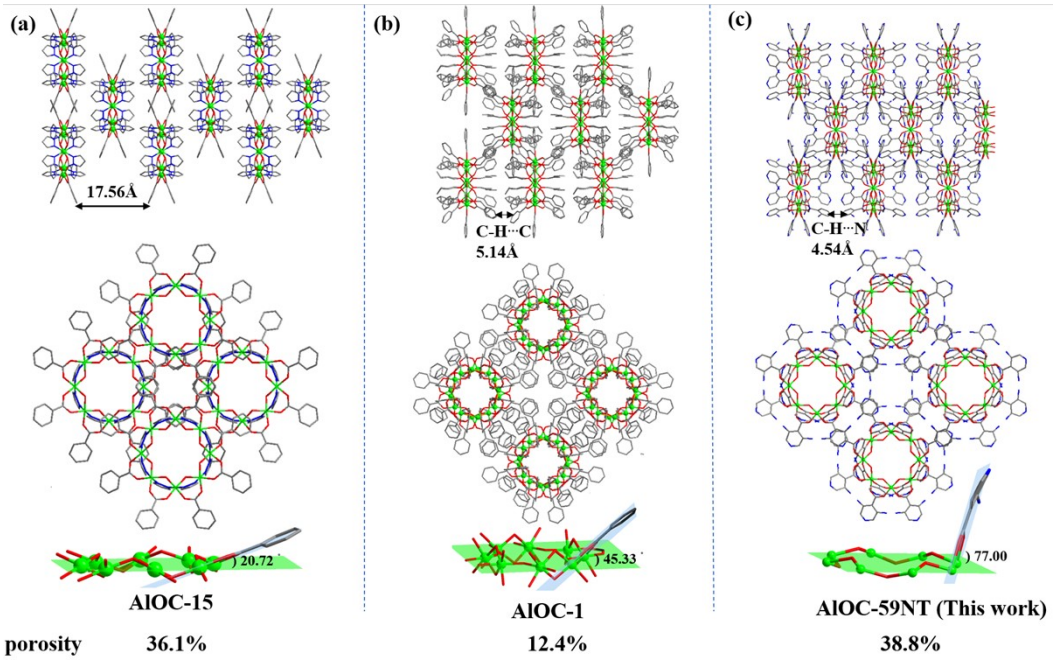

Figure S15. The summary of square nanotube arrays. (a) **AlOC-15**; (b) **AlOC-1**; (c) **AlOC-59NT.**

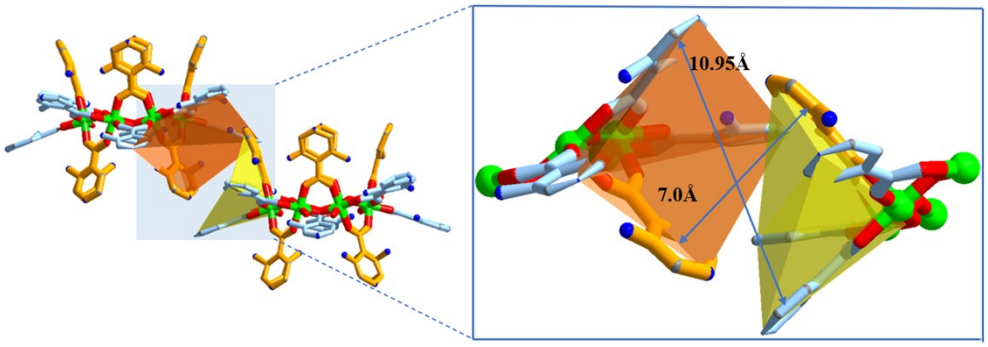

Figure S16. The side view of the peanut-shaped cavity in **AlOC-59NT** (dimension: 10.95*7.0 Å^2)**.**

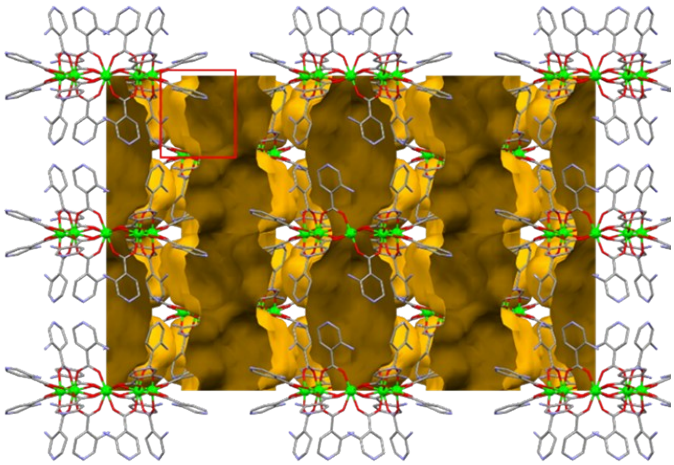

Figure S17. Side perspective view of the peanut-shaped cavity along b axis in **AlOC-59NT**.

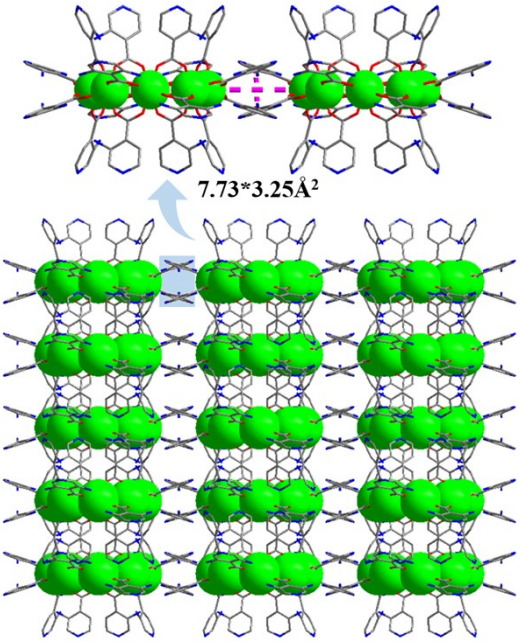

Figure S18. The ball-and-stick diagram of **AIOC-59NT** viewed along [-1 1 0].

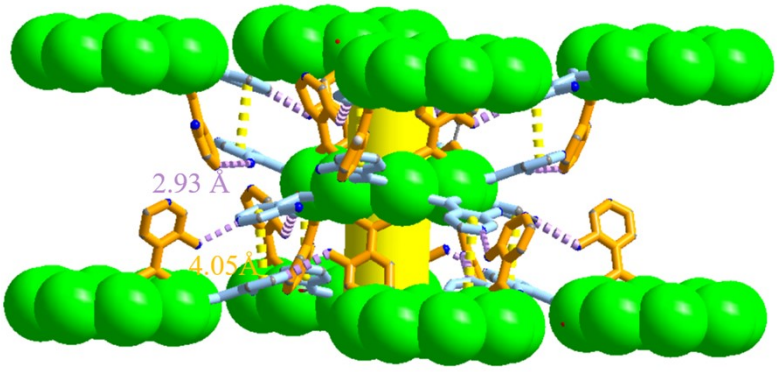

Figure S19. The interaction force between aromatic ligands on adjacent nanotubes in **AIOC-59NT**.

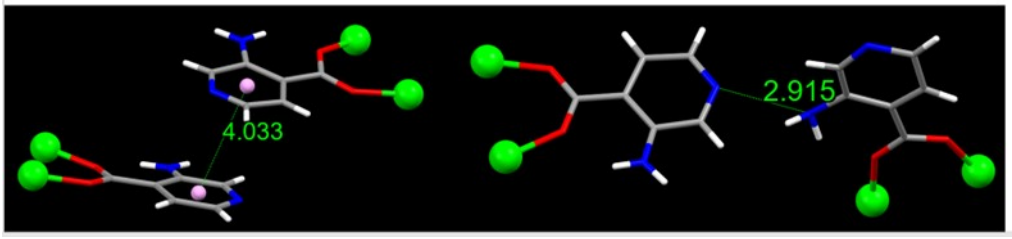

Figure S20. The supramolecular forces (π···π and hydrogen bond) between molecular rings on the adjacent nanotube. Color code: Al, green; O, red; C, gray; N, blue.

4.PXRD spectra of AlOCs

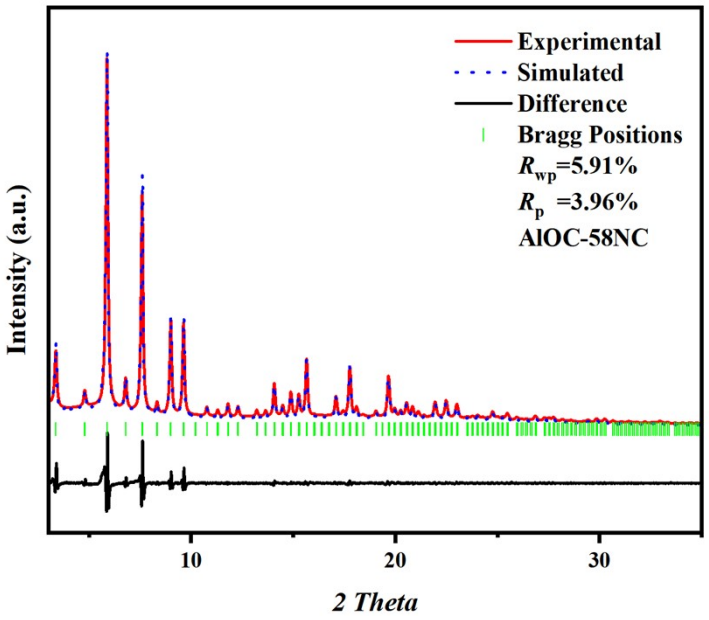

Figure S21. Pawley refinement based on PXRD of **AlOC-58NC**.

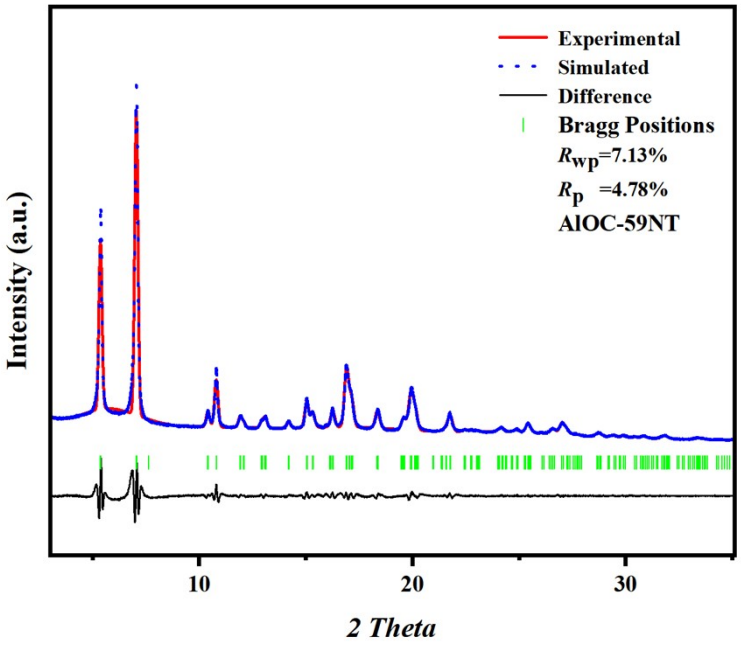

Figure S22. Pawley refinement based on PXRD of **AlOC-59NT**.

A further Rietveld refinement was performed in **AlOC-59NT** for the problem that individual experimental diffraction peaks did not appear but appeared in the simulation. As shown in Fig. S23, it was found that this problem has no major effect on the difference between experiment and simulation and agreement factors (R_p = 5.36%, R_{wp} = 7.47%).

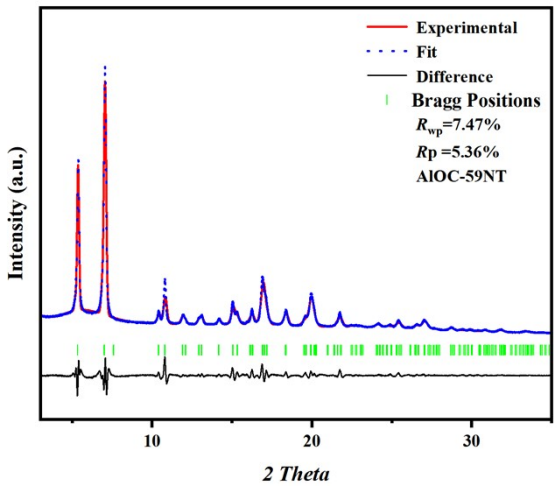

Figure S23. Rietveld refinement of **AlOC-59NT.**

5. Stability of AlOCs

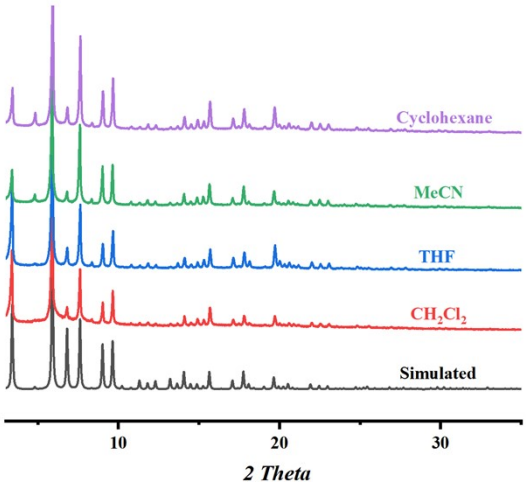

Figure S24. PXRD patterns of **AlOC-58NC** in organic solvents at room temperature for 24 h.

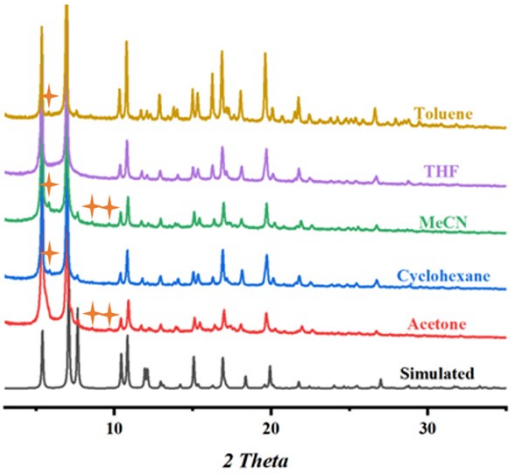

Figure S25. PXRD patterns of **AlOC-59NT** in different organic solvents at room temperature for 24 h. Although the purity of the compound is ensured by hand picking each single crystal, there are also small impurity peaks in the pattern (marked with an asterisk), which may be due to the presence of some solvent peaks.

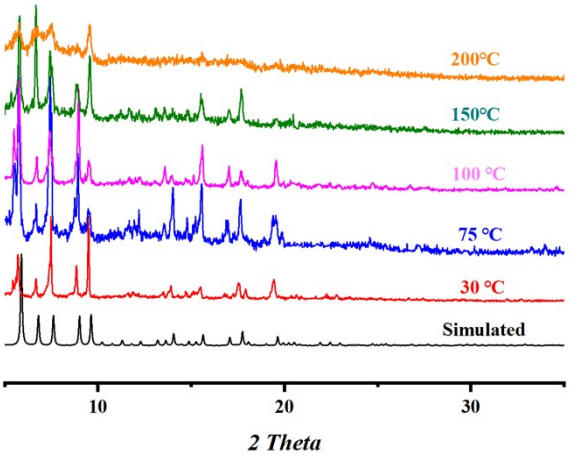

Figure S26. The Temperature-dependent PXRD patterns of **AIOC-58NC**.

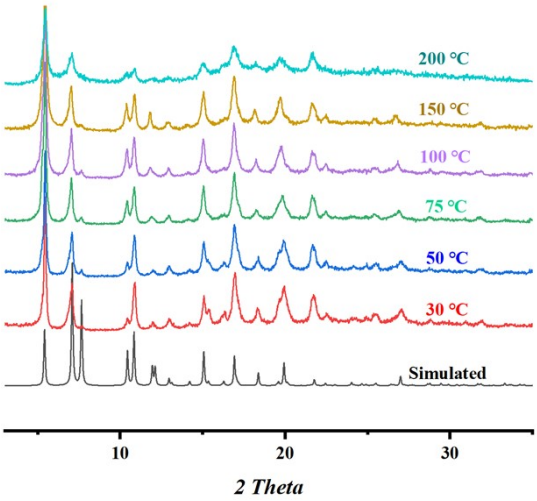

Figure S27. The Temperature-dependent PXRD patterns of **AIOC-59NT**.

6. TGA test for AIOCs

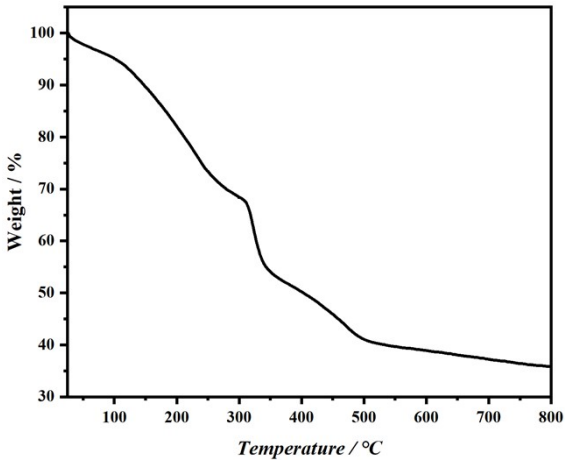

Figure S28. The TGA curve of **AIOC-58NC.**

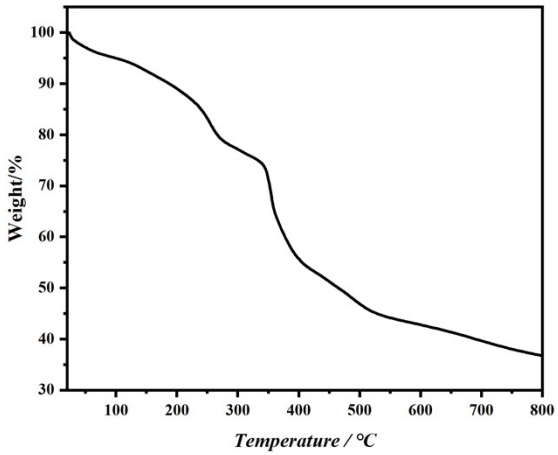

Figure S29. The TGA curve of **AIOC-59NT.**

7. The solid-state absorption spectra of AIOCs.

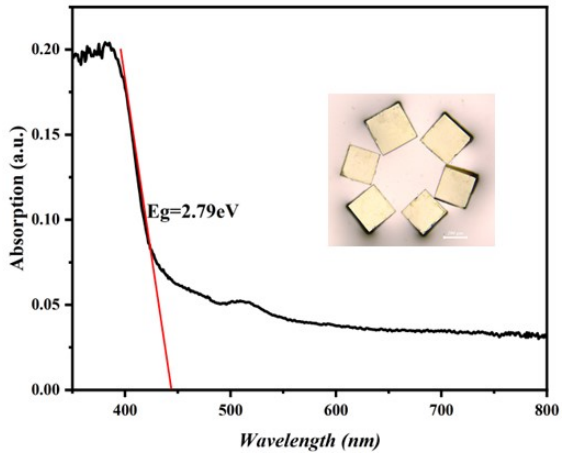

Figure S30. The solid-state absorption spectra of **AIOC-58NC**.

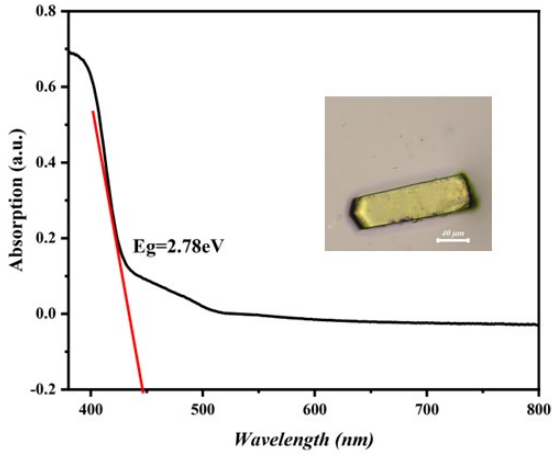

Figure S31. The solid-state absorption spectra of **AIOC-59NT**.

8. EDS spectra of AlOCs

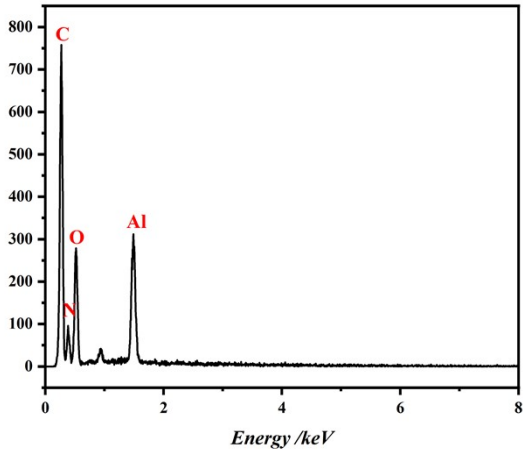

Figure S32. The EDS spectrum of compound **AlOC-58NC**.

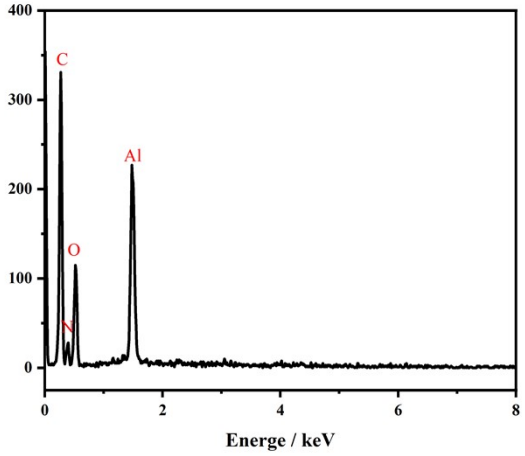

Figure S33. The EDS spectrum of compound **AlOC-59NT**.

9. FT-IR spectra of AlOCs

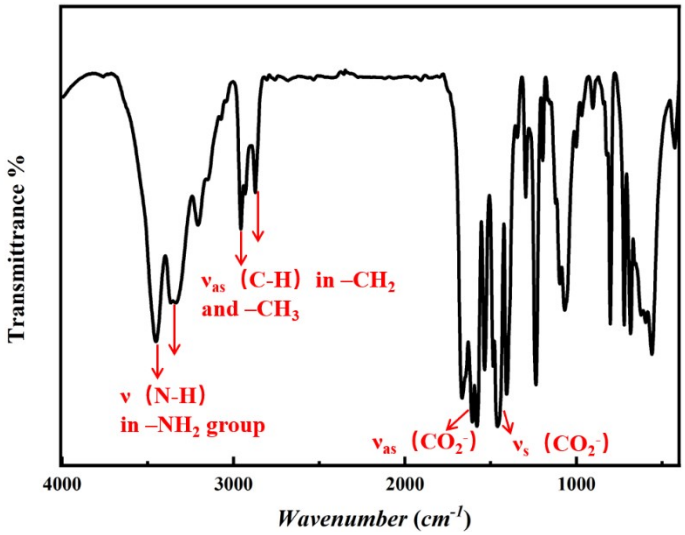

Figure S34. IR spectrum of **AlOC-58NC**.

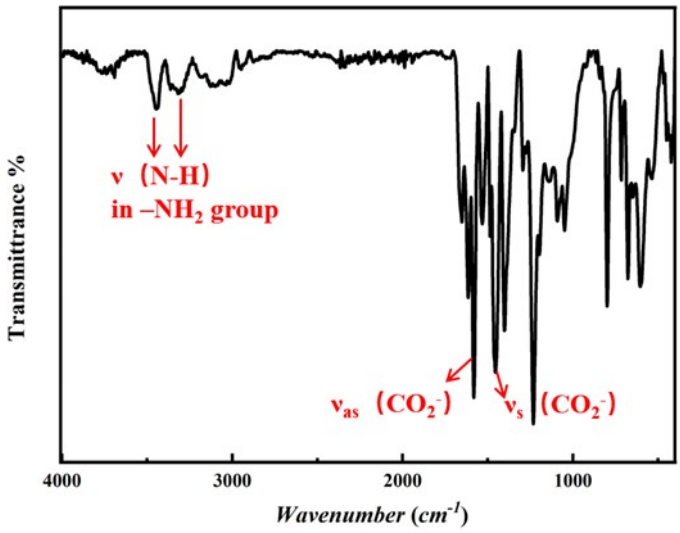

Figure S35. IR spectrum of **AlOC-59NT**.

The IR spectra of compound AlOCs have been recorded in the range of 4000–400 cm^{-1} from solid samples palletized with KBr, which are presented in Figures S34-S35. The incorporation of 3-aminoisonicotinic acid in AlOCs is supported by the C=O vibrations at 1666.47 cm^{-1} and 1449.75 cm^{-1}. The type band for the uncoordinated NH_2 group can be seen at 3453 cm^{-1} and 3349 cm^{-1}. And the aliphatic C-H stretching vibrations of the n-butoxy groups occur at about 2955 cm^{-1} and 2871 cm^{-1}.

10. Heterogeneous catalysis activity of AlOCs.

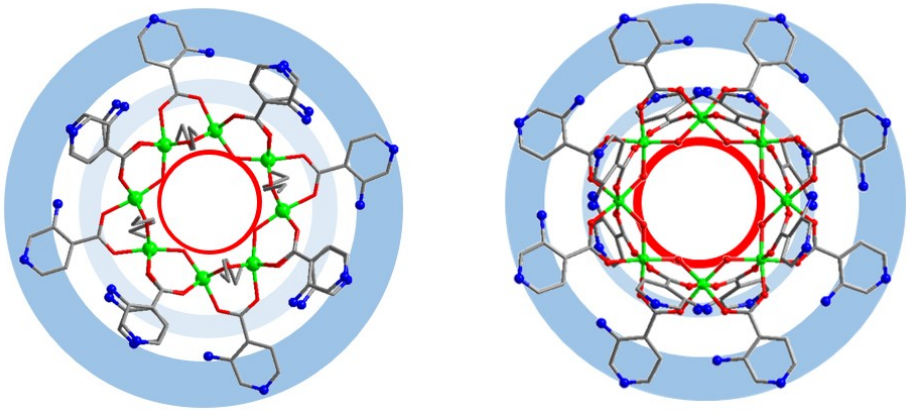

Figure 36. The abundant active sites in the porous ring structure. 4 hydroxyl groups (-OH), 12 pyridine nitrogen atoms (-Npy) and 12 amino groups (-NH_2) in **AlOC-58NC** (left). 8 hydroxyl groups (-OH), 16 pyridine nitrogen atoms (-Npy) and 16 amino groups (-NH_2) in **AlOC-59NT** (right).

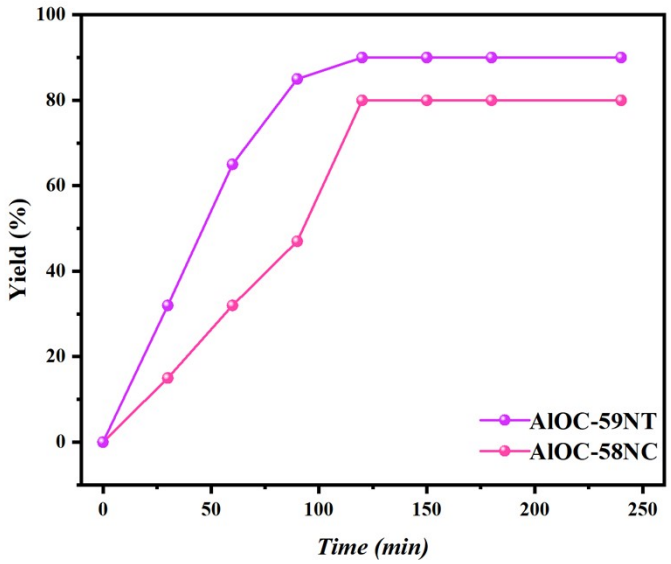

Figure S37. the reaction rate curves by using AlOCs as catalysts for the cyanosilylation reactions of benzaldehyde with TMSCN.

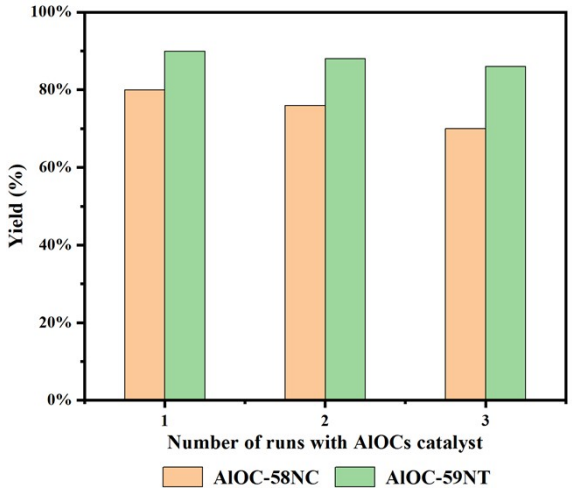

Figure S38. Recycling experiments with catalyst AlOCs for cyanosilylation reactions.

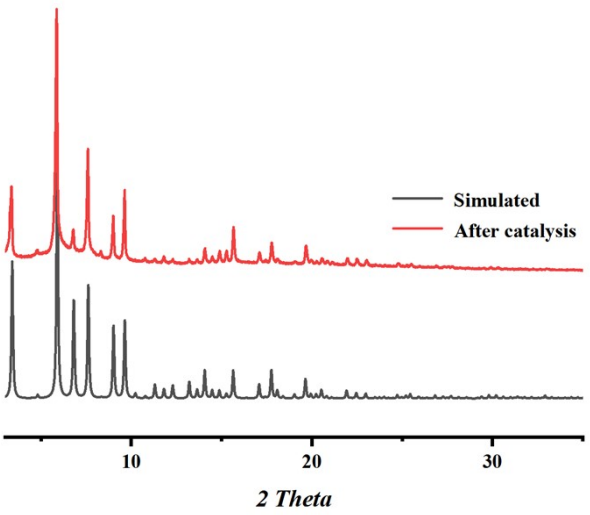

Figure S39. X-ray powder diffraction pattern of **AlOC-58NC**; simulated (black), after catalysis (red), respectively.

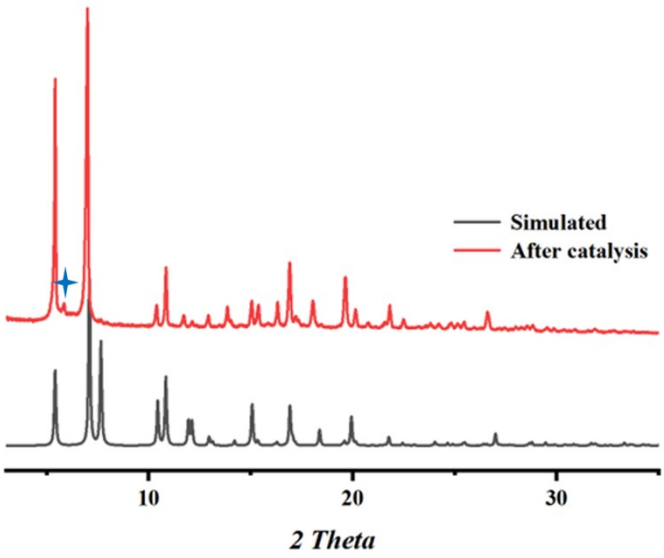

Figure S40. X-ray powder diffraction pattern of **AIOC-59NT**; simulated (black), after catalysis (red), respectively. The powder XRD pattern of the sample after catalysis has an impurity peak (marked with an asterisk) at about 6 to 7 degrees, which may be due to some solvent remaining in the structure after the catalytic reaction.

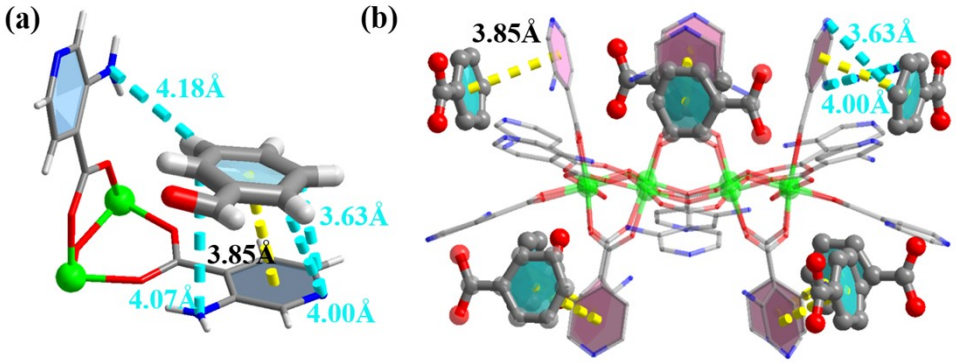

Figure S41. (a) The interaction force between the unit cell of **4Bz@AIOC-59NT** and benzaldehyde guest. (b) The interaction force between the molecular ring of **4Bz@AIOC-59NT** and eight benzaldehyde guests.

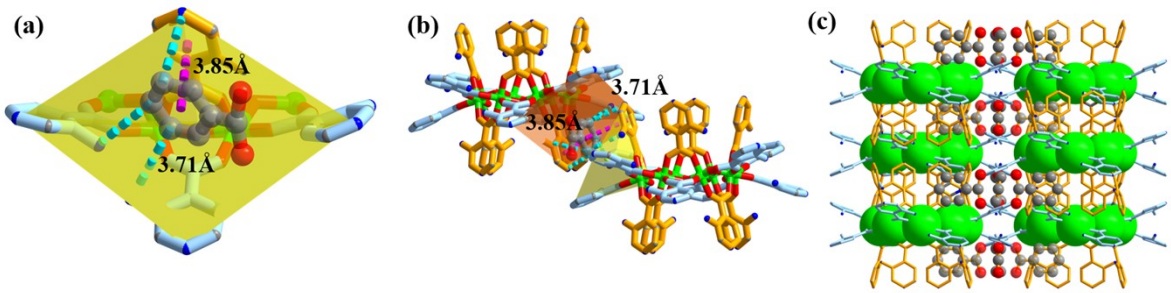

Figure S42. Distribution of benzaldehyde in (a) semi-open cavity, (b) peanut-shaped cavity, (c) the one-dimensional aromatic walls and ladders.

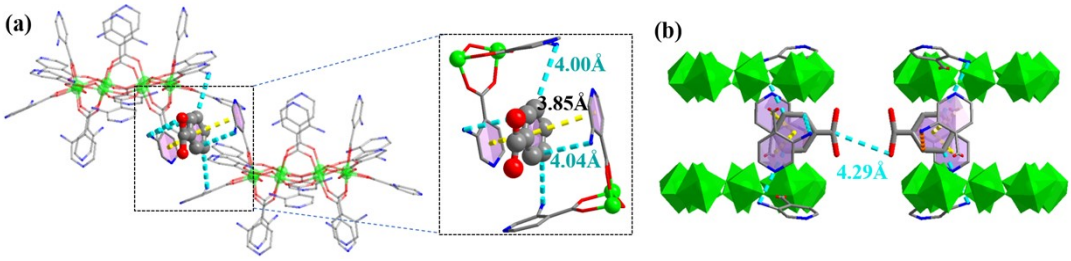

Figure S43. (a) The interaction force between benzaldehyde and the molecular ring sharing it in **4Bz@AlOC-59NT.** (b) The interaction force between adjacent benzaldehydes.

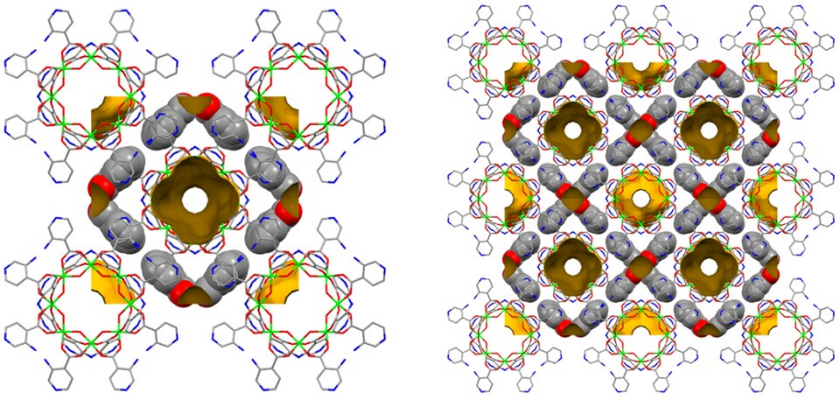

Figure S44. Perspective view of the void spaces in **4Bz@AlOC-59NT** with unit cell (left) and 2×2×2 stacking (right).

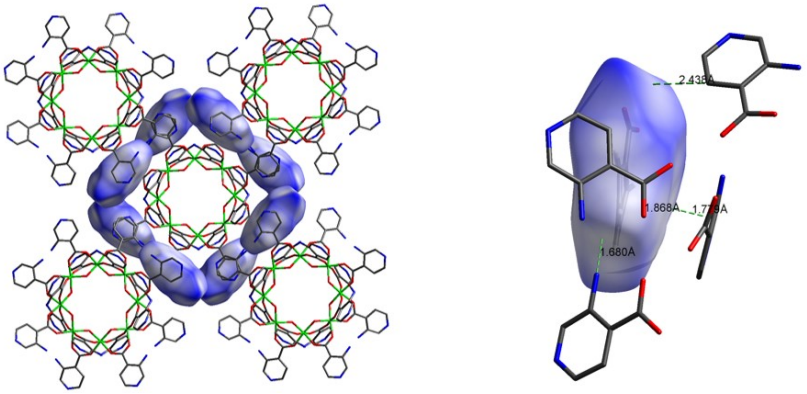

Figure S45. Hirshfeld surface analysis mapped over d_{norm} for **4Bz@AlOC-59NT.** In the color scale, negative values of d_{norm} are distinguished by contacts in red that are smaller than the van der Garde sum Walls radius. While the blue area corresponds to longer contacts with positive d_{norm} values, the white area indicates intermolecular distances close to van der Waals contacts with zero d_{norm} values.

$$d_{\text{norm}} = \frac{d_i - ri^{vdw}}{r_i^{vdw}} + \frac{d_e - re^{vdw}}{r_e^{vdw}}$$

d_e is the distance to the nearest atom external to the surface, d_i is the distance to the nearest atom internal to the surface. Both '*de*' and '*di*' and the vdW radii of the atom which are utile for the

normalized contact distance (d_{norm}) enables identification of the regions of particular importance to intermolecular interactions.

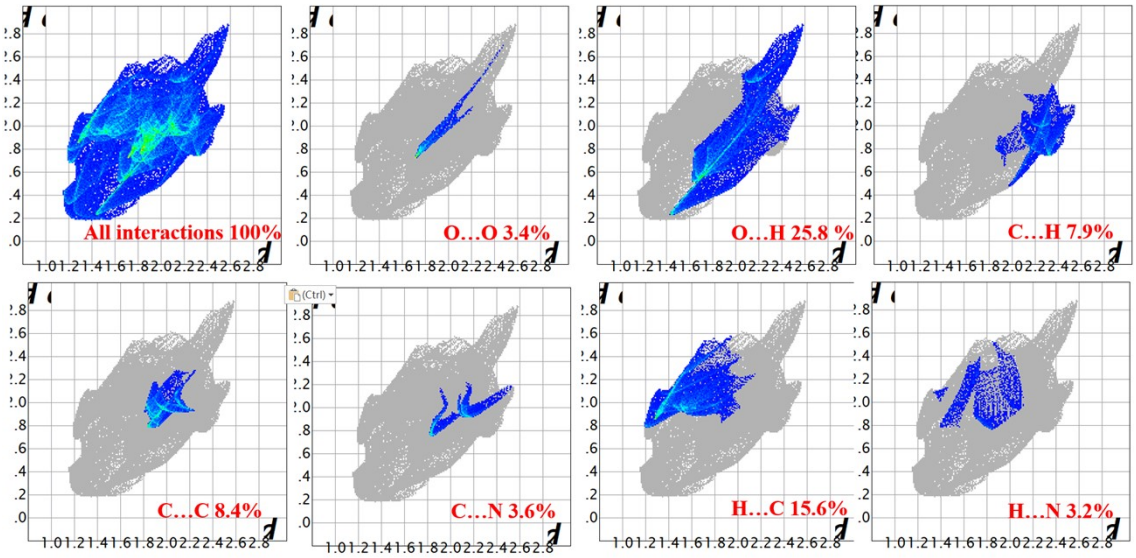

Figure S46. Fingerprint plots of major contacts in **4Bz@AlOC-59NT.**

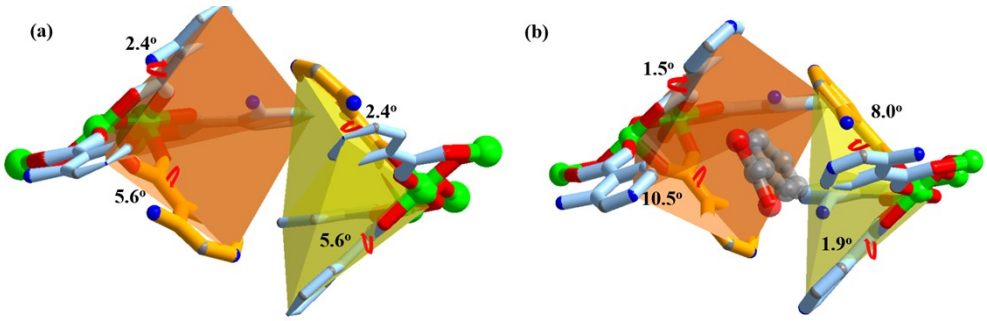

Figure S47. Changes of the torsion angle of 3-Aminoisonicotinic acid before (left) and after (right) catalytic substrate adsorption.

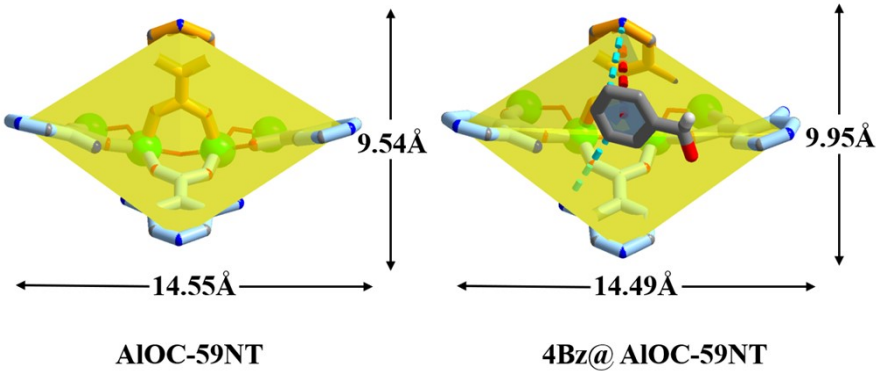

Figure S48. Change of semi-open quadrangular-conical cavity size before (left) and after (right) catalytic substrate adsorption.

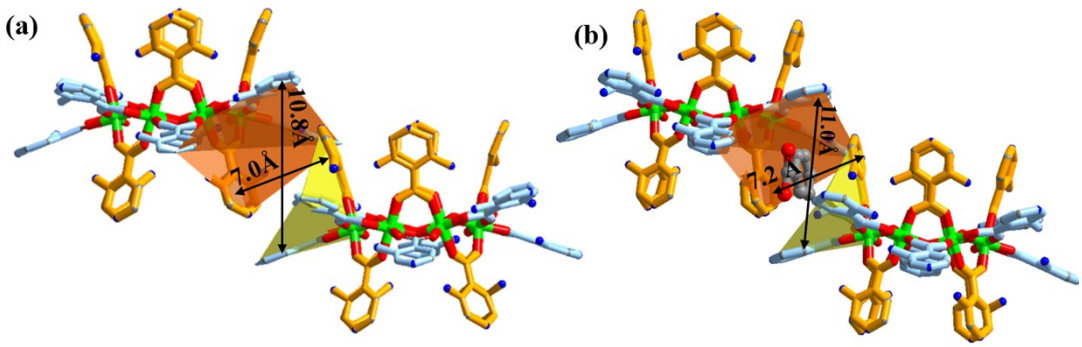

Figure S49. Change of hat-shaped cavity size before (left) and after (right) catalytic substrate adsorption.

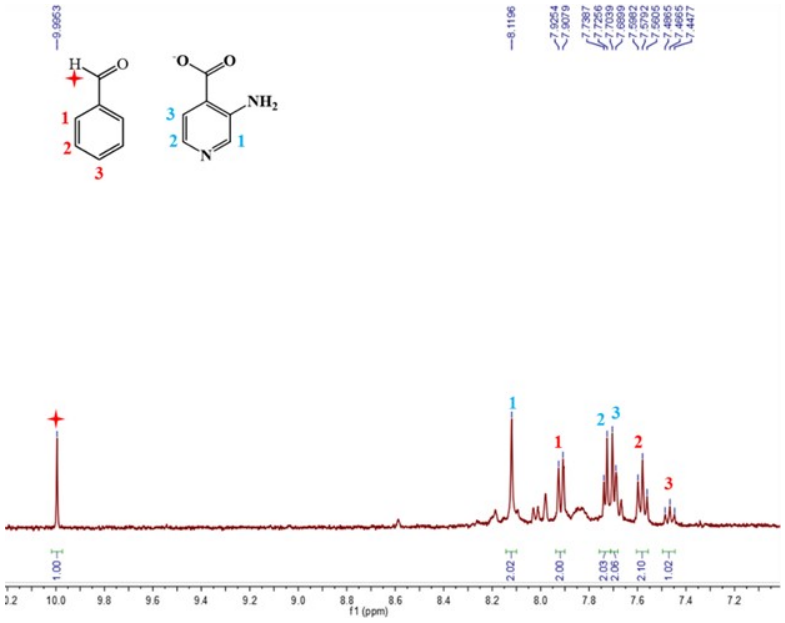

Figure S50. ^{1}H NMR spectrum of **4Bz@AIOC-59NT** in Methanol-d^{4}. (Identified the absorption peak)

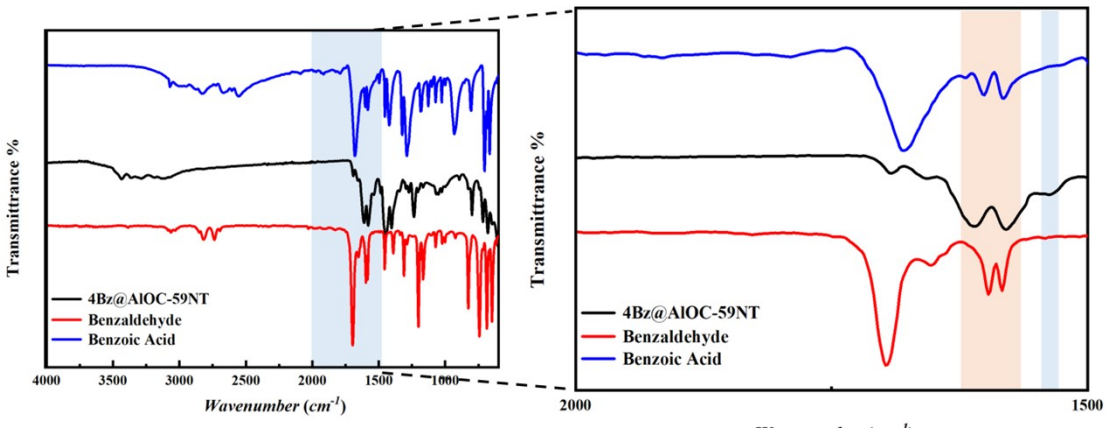

Figure S51. IR spectrum of **4Bz@AIOC-59NT**, benzaldehyde and benzoic acid.

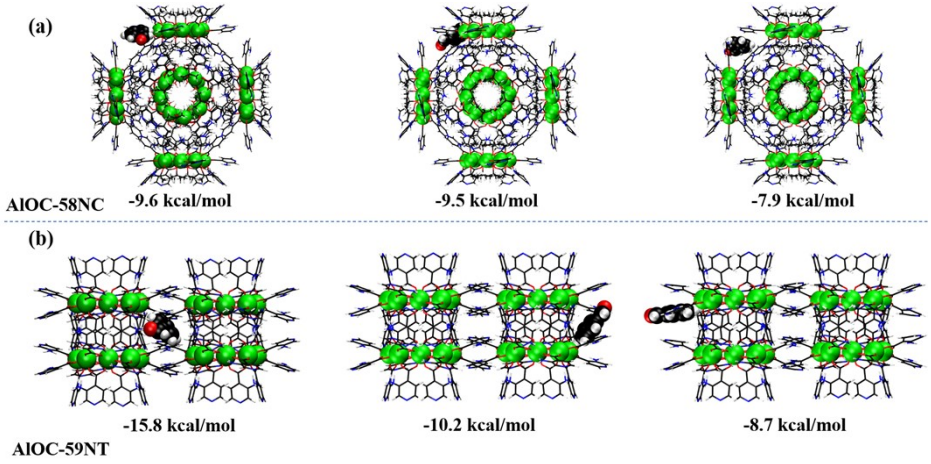

Figure S52. (a) Adsorption sites and adsorption energy in nanocages **AlOC-58NC**. (b) Adsorption sites and adsorption energy of benzaldehyde in nanotubes **AlOC-59NT**. In true crystals, the last two adsorption sites depicted in (a), which consist of only two aromatic rings, do not exist. We calculated the adsorption energies of these two adsorption sites for comparison with the first adsorption site in (a), and we discover that the presence of more aromatic rings at the adsorption sites would decrease the adsorption energy.

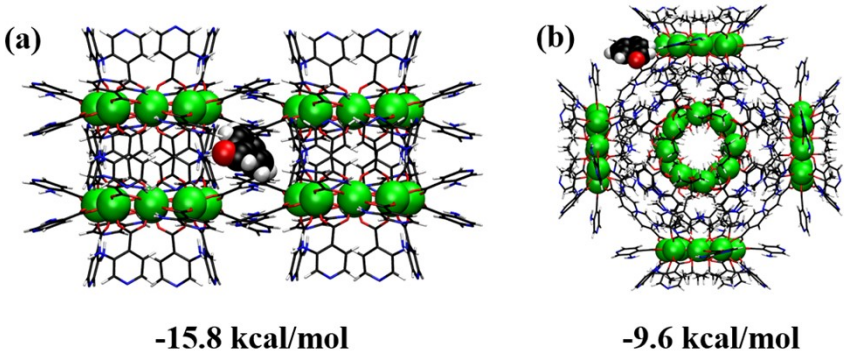

Figure S53. Comparison of adsorption energies between the most stable adsorption conformations of **AlOC-58NC** and **AlOC-59NT.**

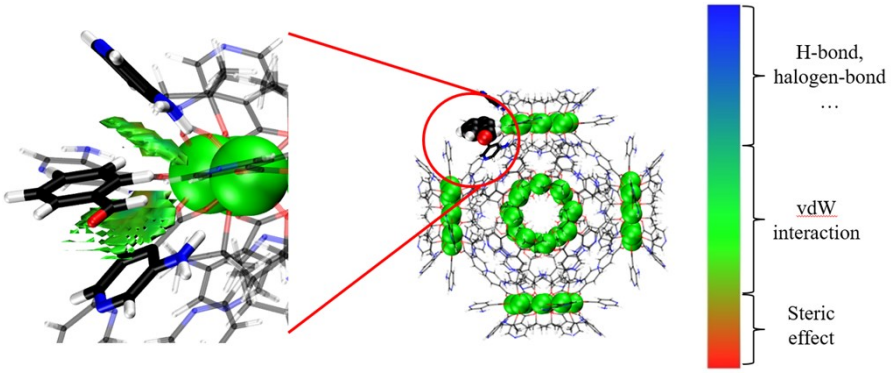

Figure S54. Adsorption site derived from theoretical calculation in **AlOC-58NC**, as well as H-bond and π-π interactions between host and guest.

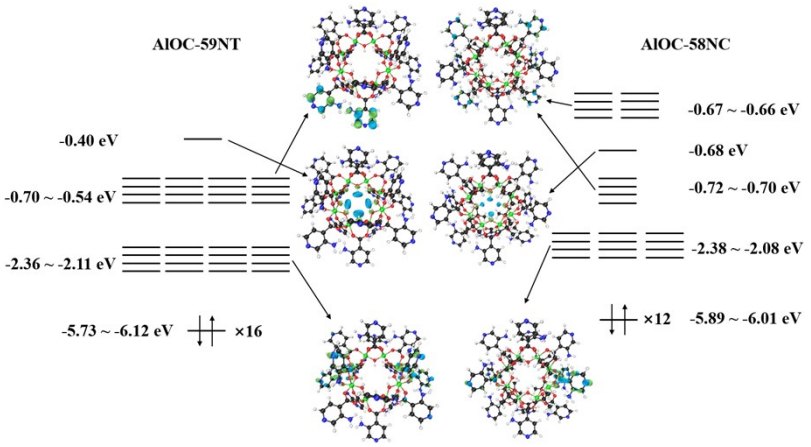

Figure S55. Energy levels of the individual monomer of **AlOC-58NC** and **AlOC-59NT**. **AlOC-59NT** has a slightly higher calculated HOMO energy levels than **AlOC-58NC**; this may indicate stronger Lewis base character of **AlOC-59NT** is slightly stronger than that of **AlOC-58NC**. On the other hand, the energy levels of their LUMOs are similar, but the higher number of LUMOs in **AlOC-59NT** may account for its slightly greater Lewis acid character. Overview, monomer of **AlOC-59NT** is calculated to have stronger Lewis acid/base characters than that of **AlOC-58NC.**

11.Supplementary tables

Table S1 Hydrogen bond parameters for AIOC-58BC

D-H···A	d(D-H)	d(D-A)	d(H-A)	<(DHA)
N00L-H00B···C00U	0.90	3.837	3.377	115
N00L-H00B···O00A	0.90	2.687	1.99	133
N00M-H00C···N00N	0.86	2.967	2.12	169
N00M-H00D···O009	0.86	2.673	2.05	128
N00M-H00D···O007	0.86	2.395	2.55	166
N00R-H00E···O00Y	0.92	3.000	2.12	161
N00R-H00F···O00C	0.94	2.675	2.08	120

Table S2 Hydrogen bond parameters for AIOC-59NT

D-H···A	d(D-H)	d(D-A)	d(H-A)	<(DHA)
N00N-H00E···O03	0.88	2.575	1.93	130
N00N-H00E···N00N	0.88	2.870	2.53	104
N00N-H00C···C00O	0.88	3.393	2.53	176
N00E-H00A···N00B	0.88	2.882	2.01	172
N00E-H00B···O07	0.88	2.672	2.05	127

Table S3 BVS analysis for AIOC-58NC

BVS Value	Bond distance		BVS Value	Bond distance	
Al01 3.2212	Al01-O04[1]	1.841(3)	Al02 3.2408	Al02-O03[2]	1.903(3)
	Al01-O04	1.841(3)		Al02-O03	1.903(3)
	Al01-O05[1]	1.907(3)		Al02-O04	1.840(3)
	Al01-O05	1.907(3)		Al02-O04[2]	1.840(3)
	Al01-O07[1]	1.899(3)		Al02-O06[2]	1.897(3)
	Al01-O07	1.899(3)		Al02-O06	1.897 (3)

System code: [1]+X, 1-Y ,1-Z; [2]1-Y, 1-X, 1-Z.

Table S4 BVS analysis for AIOC-59NT.

BVS Value	Bond distance		BVS Value	Bond distance	
Al01 3.0949	Al01-O04	1.873(3)	Al02 3.0644	Al02-O04[2]	1.878(3)
	Al01-O05	1.876(3)		Al02-O05[2]	1.879(3)
	Al01-O06	1.847(3)		Al02-O06	1.852(3)
	Al01-O007[1]	1.976(3)		Al02-O008	1.925(3)
	Al01-O009	1.917(3)		Al02-O00A	1.951(3)
	Al01-O00C	1.900(3)		Al02-O00B	1.922(4)

System code: [1]+X, +Z, 1-Y; [2]+X, 1-Z, +Y.

Table S5 catalytic activity of several heterogeneous catalysts used in the cyanosilylation of aldehyde

Catalyst	Reaction conditions	Time and yield	Reference
Al-ITO-NO_2	Benzaldehyde (5mmol) TMSCN(6mmol) 0.5mol% Al 303K	5h, 100%	12
Al-ITO-Br		5h, 88%	
InPF-16	Benzaldehyde (1mmol) TMSCN(1mmol) 1mol% for benzaldehyde 298K	0.17h, 99%	13
InPF-17		18h, 67%	
1	Benzaldehyde (0.5mmol) TMSCN(1.5mmol) 2mol% for benzaldehyde 323K	4h, 99.2%	14
NUS-50-Co	Benzaldehyde (1mmol) TMSCN(1.2mmol) 2.5mol% for benzaldehyde 298K	10h, 98%	15
Y-POM	Benzaldehyde (0.5mmol) TMSCN(0.75mmol) 1mol% for benzaldehyde 298K	6h, 75%	16
$[Ag_4(apym)_4(SiW_{12}O_{40})]_n$	Benzaldehyde (0.5mmol) TMSCN(1mmol) 0.1mol% for benzaldehyde 303K	4h, 96.2%	17
1	Benzaldehyde (0.5mmol) TMSCN(0.75mmol) 0.1mmol 303K	4h, 99%	18
2		4h, 90%	
Ru-catalyst	Benzaldehyde (1mmol) TMSCN(1.5mmol) 0.5mol% 303K	6h, 99%	19
Co-MOF	Benzaldehyde (0.5mmol) TMSCN(1mmol) 0.1mmol % 303K	12h, 98%	20
1	Benzaldehyde (1mmol) TMSCN(2mmol) 0.5mol % 303K	3h, 86%	21
2		3h, 52%	
3		3h, 61%	
$[(AT)Al(DMAP)]^+[OTf]^-$	Benzaldehyde (1 mmol) TMSCN (1.2 mmol) 2 mol% 303K	30 min, 95%	22
1	Benzaldehyde (0.5 mmol) TMSCN (0.75 mmol) 0.1 mol% 303K	10 min, 99%	23

Table S6 Substrate scope for cyanosilylation of aldehyde compound with TMSCN catalyzed by AlOCs.[a]

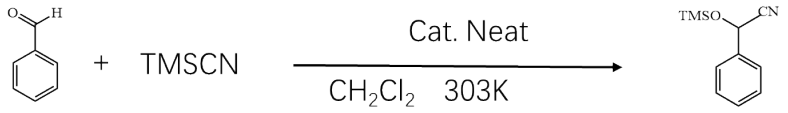

Entry	Catalytic	Substrate	Time (h)	Yield (%) [b]
1	**AlOC-58NC**	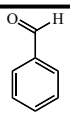	2	80
2	**AlOC-59NT**		2	92
3	blank		2	Trace
4	$Al(O^iPr)_3$	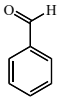	2	48
5	3-aminoisonicotinic acid		2	Trace
6	**AlOC-58NC**	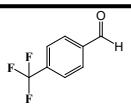	2	85
7	**AlOC-59NT**		2	96
8	**AlOC-58NC**	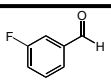	2	82
9	**AlOC-59NT**		2	92
10	**AlOC-58NC**	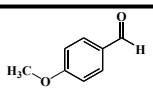	2	57
11	**AlOC-59NT**		2	70
12	**AlOC-58NC**	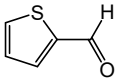	2	65
13	**AlOC-59NT**		2	65
14	**AlOC-58NC**		2	73
15	**AlOC-59NT**		2	86

[a]Reaction conditions: catalyst **AlOC-58NC** and **AlOC-59NT**, 1.5 mol%, aldehyde 0.5 mmol, TMSCN 1 mmol, CH_2Cl_2 as solvent, temperature (303 K) under N_2. [b] Yields were determined by ^1H NMR using CH_2Br_2 as an internal standard.

Table S7. Experimental single-crystal X-ray data for AlOC-58NC and AlOC-58NC-1.

	AlOC-58NC	AlOC-58NC-1
Empirical formula	$Al_8C_{104}N_{24}O_{36}H_{136}$	$Al_8C_{104}N_{24}O_{36}H_{136}$
Formula weight	2514.18	2514.18
Temperature / K	100	100
Crystal system	cubic	cubic
Space group	*I*432	*I*432
a [Å]	36.6848(4)	36.6170(3)
b [Å]	36.6848(4)	36.6170(3)
c [Å]	36.6848(4)	36.6170(3)
α [◦]	90	90
β [◦]	90	90
γ [◦]	90	90
V [Å ^{3}]	49369.5(16)	49096.2(12)
Z	12	12
ρcalcd [g cm^{-3}]	0.953	0.923
μ [mm^{-1}]	0.656	0.998
F (000)	14400.0	14112.0
Index ranges	-31 ≤ h ≤ 33 -39 ≤ k ≤ 44 -41≤ l ≤ 47	-42≤ h ≤45 -41 ≤ k ≤ 44 -45 ≤ l ≤35
Reflections collected	35811	155022
Independent refs [R_{int}]	9372 [0.0538]	8511[0.0719]
date/restraints/parameters	9372/20/378	8511/18/370
Goodness-of-fit on F^2	1.167	1.009
R_1[a], wR_2[b] [I>2σ(I)]	0.0852, 0.2158	0.0521, 0.1355
R_1, wR_2 [all data]	0.1000, 0.2245	0.0570, 0.1392
CCDC number	2214966	2214968

[a]$R_1 = \Sigma||F_o|-|F_c||/\Sigma|F_o|$. [b]$wR_2 = \{\Sigma[w(F_o^2-F_c^2)^2]/\Sigma[w(F_o^2)^2]\}^{1/2}$

Table S8. Experimental single-crystal X-ray data for AIOC-59NT and 4Bz@AIOC-59NT.

	AIOC-59NT	4Bz@AIOC-59NT
Empirical formula	$Al_8C_{96}N_{32}O_{40}H_{88}$	$Al_8C_{124}N_{32}O_{44}H_{112}$
Formula weight	2537.76	2970.25
Temperature / K	100.00(10)	100.00(10)
Crystal system	tetragonal	tetragonal
Space group	*I*422	*I*422
a [Å]	23.0719(3)	22.8500(3)
b [Å]	23.0719(3)	22.8500(3)
c [Å]	14.7983(4)	14.9095(4)
α [◦]	90	90
β [◦]	90	90
γ [◦]	90	90
V [Å ^{3}]	7877.3(3)	7784.6(3)
Z	2	2
ρcalcd [g cm^{-3}]	1.070	1.262
μ [mm^{-1}]	0.720	1.230
F (000)	2608.0	3048.0
Index ranges	-30 ≤ h ≤ 28 -29 ≤ k ≤ 24 -9≤ l ≤ 19	-28 ≤ h ≤28 -21 ≤ k ≤ 27 -18 ≤ l ≤13
Reflections collected	14401	19245
Independent refs [R_{int}]	4441 [0.0451]	3983[0.0369]
date/restraints/parameters	4441/37/188	3983/63/230
Goodness-of-fit on F^2	0.988	1.210
R_1[a], wR_2[b] [I>2σ(I)]	0.0707, 0.2046	0.0967, 0.2670
R_1, wR_2 [all data]	0.0842, 0.2193	0.1055, 0.2804
CCDC number	2214967	2214969

[a]$R_1 = \Sigma||F_o|-|F_c||/\Sigma|F_o|$. [b]$wR_2 = \{\Sigma[w(F_o^2-F_c^2)^2]/\Sigma[w(F_o^2)^2]\}^{1/2}$

12. Reference

[1]. G. M. Sheldrick, *Acta Cryst. C.* 2015, **71**, 3-8.

[2]. S. Spicher and S. Grimme, *Angew. Chem. Int. Ed.* 2020, **59**, 15665-15673.

[3]. E. C. Philipp Pracht, S. Ehlert, and S. Grimme, *chemRxiv* 2019, 1-19.

[4]. E. C. Christoph Bannwarth, S. Ehlert, A. Hansen, P. Pracht, J. Seibert, S. Spicher, S. Grimme, *WIREs Comput. Mol. Sci.* 2020, **11**, 1-49.

[5]. C. Bannwarth, S. Ehlert and S. Grimme, *J. Chem. Theory Comput.* 2019, **15**, 1652-1671.

[6]. (a) J. Tao, J. P. Perdew, V. N. Staroverov and G. E. Scuseria, *Phys. Rev. Lett.* 2003, **91**, 146401; (b) G. E. S. Viktor and N. Staroverova, *J. Chem. Phys.* 2004, **121**, 11507.

[7]. F. Weigend and R. Ahlrichs, *Phys. Chem. Chem. Phys.* 2005, **7**, 3297-3305.

[8]. (a) F. Neese, F. Wennmohs, U. Becker and C. Riplinger, *J. Chem. Phys.* 2020, **152**, 224108; (b) F. Neese, *WIREs Comput. Mol. Sci.* 2022, **12**; (c) F. Neese, *WIREs Comput. Mol. Sci.* 2011, **2**, 73-78.

[9]. T. Lu and F. Chen, *J. Comput. Chem.* 2012, **33**, 580-592.

[10]. T. Lu and Q. X. Chen, *Chem. Methods* 2021, **1**, 231–239.

[11]. S. S. Yao, W. H. Fang, Y. Sun, S. T. Wang and J. Zhang, *J. Am. Chem. Soc.* 2021, **143**, 2325-2330.

[12]. J. M. Frost, R. J. Stirling, S. Sanz, N. Vyas, G. S. Nichol, G. Rajaraman and E. K. Brechin, *Dalton Trans.* 2015, **44**, 10177-10187.

[13]. L. M. Aguirre-Diaz, M. Iglesias, N. Snejko, E. Gutierrez-Puebla and M. A. Monge, *Chem. Eur. J.* 2016, **22**, 6654-65.

[14]. H. An, Y. Zhang, Y. Hou, T. Hu, W. Yang, S. Chang and J. Zhang, *Dalton Trans.* 2018, **47**, 9079-9089.

[15]. T. Kundu, J. Wang, Y. Cheng, Y. Du, Y. Qian, G. Liu and D. Zhao, *Dalton Trans.* 2018, **47**, 13824-13829.

[16]. S. Li, Y. Zhou, Q. Peng, R. Wang, X. Feng, S. Liu, X. Ma, N. Ma, J. Zhang, Y. Chang, Z. Zheng and X. Chen, *Inorg. Chem.* 2018, **57**, 6624-6631.

[17]. T. P. Hu, Y. Q. Zhao, K. Mei, S. J. Lin, X. P. Wang and D. Sun, *CrystEngComm* 2015, **17**, 5947-5952.

[18]. T. Rom and A. K. Paul, *Dalton Trans.* 2020, **49**, 13618-13634.

[19]. G. Vinoth, S. Indira, M. Bharathi, L. G. Alves, A. M. Martins and K. Shanmuga Bharathi, *Inorganica Chim. Acta* 2021, **514**, 120006-120013.

[20]. X. Cui, M. C. Xu, L. J. Zhang, R. X. Yao and X. M. Zhang, *Dalton Trans.* 2015, **44**, 12711-12716.

[21]. Y. Jiang, R. Liu, Y. Gong, Y. Fan, L. Wang and J. Xu, *Dalton Trans.* 2021, **50**, 9540-9546.

[22]. M. K. Sharma, S. Sinhababu, G. Mukherjee, G. Rajaraman and S. Nagendran, *Dalton Trans.* 2017, **46**, 7672-7676.

[23]. W. Wang, M. Luo, J. Li, S. A. Pullarkat and M. Ma, *Chem. Commun.* 2018, **54**, 3042-3044.